technologies

MDPI

*Article*

# Green Methodology for Producing Bioactive Nanocomposites of Mesoporous Silica Support for Silver and Gold Nanoparticles Against *E. coli* and *S. aureus*

**Una Stamenović [1,*], Dijana Mašojević [1], Maja Kokunešoski [1], Mojca Otoničar [2], Slađana Davidović [3], Srečo Škapin [2], Tanja Barudžija [1], Dejan Pjević [1], Tamara Minović Arsić [1] and Vesna Vodnik [1,*]**

[1] Vinča Institute of Nuclear Sciences—National Institute of the Republic of Serbia, University of Belgrade, 11351 Belgrade, Serbia; dijanamasojevic@gmail.com (D.M.); majako@vin.bg.ac.rs (M.K.); tbarudzija@vin.bg.ac.rs (T.B.); dejanp@vinca.rs (D.P.); tamaraminovic@vin.bg.ac.rs (T.M.A.)
[2] Jožef Štefan Institute, 1000 Ljubljana, Slovenia; mojca.otonicar@ijs.si (M.O.); sreco.skapin@ijs.si (S.Š.)
[3] Faculty of Technology and Metallurgy, University of Belgrade, 11000 Belgrade, Serbia; sdavidovic@tmf.bg.ac.rs
* Correspondence: una.bogdanovic@gmail.com (U.S.); vodves@vin.bg.ac.rs (V.V.)

**Abstract**

This study considered and compared silver, gold, and their combination of nanoparticles (AgNPs, AuNPs, and Au-AgNPs) with biocompatible material mesoporous silica SBA-15 as potential antibacterial agents. A facile, one-pot "green" methodology, utilizing L-histidine as a reducing agent and bridge between components, was employed to obtain Ag@SBA-15, Au@SBA-15, and Au-Ag@SBA-15 nanocomposites without the use of external additives. Various physicochemical tools (UV-Vis, TEM, SAED, FESEM, XPS, BET, XRD, and FTIR) presented SBA-15 as a good carrier for spherical AgNPs, AuNPs, and Au-AgNPs with average diameters of 8.5, 16, and 9 nm, respectively. Antibacterial evaluations of *Escherichia coli* and *Staphylococcus aureus* showed that only Ag@SBA-15, at a very low Ag concentration (1 ppm) during 2 h of contact, completely reduced the growth (99.99%) of both strains, while the Au@SBA-15 nanocomposite required higher concentrations (5 ppm) and time (4 h) to reduce 99.98% *E. coli* and 94.54% *S. aureus*. However, Au introduction in Ag@SBA-15 to form Au-Ag@SBA-15 negatively affected its antibacterial potential, lowering it due to the galvanic replacement reaction. Nevertheless, the rapid and effective combating of two bacteria at low NPs concentrations, through the synergistic effects of mesoporous silica and AgNPs or AuNPs, in Ag@SBA-15 and Au@SBA-15 nanocomposites, provides a potential substitute for existing bacterial disinfectants.

**Keywords:** green methodology; silver nanoparticles; gold nanoparticles; mesoporous silica; nanocomposite; bacteria inhibition

Academic Editor: Miklas Scholz

Received: 16 July 2025
Revised: 3 October 2025
Accepted: 7 October 2025
Published: 9 October 2025

**Citation:** Stamenović, U.; Mašojević, D.; Kokunešoski, M.; Otoničar, M.; Davidović, S.; Škapin, S.; Barudžija, T.; Pjević, D.; Arsić, T.M.; Vodnik, V. Green Methodology for Producing Bioactive Nanocomposites of Mesoporous Silica Support for Silver and Gold Nanoparticles Against *E. coli* and *S. aureus*. *Technologies* **2025**, *13*, 458. https://doi.org/10.3390/technologies13100458



## 1. Introduction

The rapid rise in antibiotic resistance has become a serious and complex public health problem today due to the numerous defense mechanisms that microorganisms have developed to counteract antimicrobial agents, whose effectiveness is compromised [1]. A particularly urgent problem arises when microbes deploy resistance faster than new antimicrobials (antibiotics, antivirals, antifungals, and antiparasitic agents) can be developed. Among bacteria, for example, methicillin-resistant *S. aureus* is one of the most

dangerous resistant bacteria, which can easily infect humans during prolonged hospital stays and unsanitary medical conditions, causing numerous health problems [2]. Additionally, due to antibiotic resistance to third-generation cephalosporins (a commonly prescribed antibiotic), even non-pathogenic *E. coli* strains have now become pathogenic [3]. However, we must keep in mind that the evolution of resistance in bacteria is a natural process that develops genetically, either through mutation or with the acquisition of new resistance genes through the genetic exchange [4]. Therefore, there is a growing global need for more advanced antimicrobials that could overcome and/or improve the characteristics of existing ones. These materials should satisfy a few criteria: to be biocompatible, low-cost materials, to possess excellent abilities for long-term treatment efficacy with no side effects, to be highly effective against various resistant strains, and to have rapid activity at low concentrations. However, even though numerous steps have not yet been simultaneously fulfilled, these conditions motivate researchers to create new materials, especially using nanomaterials for this purpose due to their abundant surface chemistry and high surface-to-volume ratio, sorption capacity, and selectivity for target microbes [5–7]. The new materials, among others, based on mesoporous silica particles (MSPs) and metal nanoparticles (MetNPs), have some advantages [8–11]. The MSPs are appealing materials owing to their periodically aligned pore structure with tunable pore size (2–50 nm) and particle dimensions (50–300 nm), high surface area (500–1000 $m^2/g$) and pore volumes (0.6–1 $cm^3/g$), high density of surface silanol groups, relatively high hydrothermal stability (≤100 °C), good biodegradability/biocompatibility, as well as improved acid–base tolerance [8,12]. For example, a high surface area should provide a large number of reaction sites for surface-related processes, large pore volumes provide loading of guest species, while tunable mesopore channels facilitate the transport of ions, molecules, or nanoparticles through the bulk of the material. Extensive efforts have been made towards exploring these materials as carriers for various agents due to their easy surface functionalization for immobilizing or encapsulating therapeutic molecules, as well as safeguarding the sensitive guest molecules [8,13–17]. These features are particularly advantageous for the attachment of well-known bactericides, such as MetNPs and their oxides/ions (CuNPs, AgNPs, CuONPs, $Ag_2$ONPs, and AuNPs) for the purpose of designing hybrid organic/inorganic nanomaterials as powerful structures for different applications—nanocarriers for controlled drug delivery and release, imaging, sensing, etc. [8,11,18–20]. In addition, among these nanomaterial-based treatments, photothermal applications of Au–mesoporous silica as photostimuli-responsive nanomaterials or a Ag-based nanoplatform for chemo-/photodynamic therapy against drug-resistant bacterial infections in deep tissues are also attractive due to their obvious advantages of effective intercellular penetration and minimum invasiveness [21,22]. The large surface reactivity of these NPs, attributed to a high percentage of unsaturated surface atoms that tend to interact with the surrounding media, enables them to undergo better uptake by cells and tissues via endocytosis and other pathways compared to classical treatments [23–26]. In this context, their broad investigation for antimicrobial purposes is a consequence of their interaction with both eukaryotic and prokaryotic cells, exerting powerful toxic effects against a wide range of pathogenic organisms. On the other hand, the spatially selective functionalization of the internal pore system or external particle surface of MSPs with organic/inorganic moieties is often an essential requirement for their interactions with the environment (specific cell targeting or attaching various species), providing prolonged stability of MSPs in biological media [27]. For example, Slowing et al. demonstrated that MSPs with negatively charged surface functionalization escape more easily from the endosomes of cancer cells due to their high buffering capacity, facilitating the delivery of therapeutic agents from the endosome to the cytoplasm and thereby enhancing their effectiveness for cancer treatment [28]. In addition, the functionalization of MSPs by amino acids enhances their

characteristics by providing additional sites, in the form of amino or carboxyl groups, for coupling with surrounding ions and biomolecules, and in our case, with MetNPs. Moreover, it is important from MetNPs' point of view, since certain functional groups, such as indole, phenol, and imidazole from tryptophan, tyrosine, and histidine, respectively, can easily reduce metal ions to atoms and further to nanoparticles, capping them, and enhancing their biological activity [29,30]. Using amino acids for MetNPs' preparation is environmentally friendly, practical, and can be useful for food technology and medicine. Among them, L-histidine has the highest antioxidant activity compared to the other essential amino acids and is the greatest reducing and capping agent [31]. Bearing this in mind, here we demonstrate a novel, green methodology for the fabrication of nanocomposites—histidine-functionalized mesoporous silica SBA-15 doped with AgNPs, AuNPs, or Au-AgNPs—to minimize the environmental impact and investigate their toxicity against multidrug-resistant bacteria, *E. coli* and *S. aureus,* as models of living organisms. Mesoporous silica SBA-15 functionalized by histidine was used as a surface to obtain in situ metal NPs and form nanocomposites. To the best of our knowledge, this approach has not yet been presented in the available literature. Unlike similar presented research with more complex synthetic procedures, such as coiled flow inverter reactor for Ag-SBA15 nanocomposite preparation [32] or utilization of toxic components (3-mercaptopropyltriethoxy silane (MPTES) and 3-aminopropyltriethoxy silane (APTES)) for SBA15 functionalization and subsequent assembly of AuNPs [33], this work aims to use non-harmful and surroundings-safe L-histidine as the SBA-15 functionalizer, and low initial $AgNO_3$ and $HAuCl_4$ precursor concentrations (1 mM of the order of magnitude) to avoid environmental toxicity and prepare nanocomposites with silica in order to study their antibacterial activity. It enabled the formation of the functionalized structures with high surface area, which interact with bacteria's cell walls, disabling their functions, leading to final microbial death. In addition to this efficacy, it was also important to determine how quickly these composites could reach maximum microbial reduction at these concentrations, under conditions where this is essential. Actually, several types of Ag or Au-SBA15 nanocomposites have been investigated for their antimicrobial activity [34–38]. Most of the reported examples are based on Ag-SBA15 nanocomposites, and only a few of Au-SBA15 nanocomposites, since the AuNPs are less efficient than AgNPs, and they have enhanced antimicrobial properties when photothermally functionalized or bound to antibiotics. Various synthetic methods have been used to obtain these nanocomposites, and as a result, differences in size, shape, and content of NPs may contribute to differences in their antibacterial efficacy [39,40]. Moreover, this efficacy largely depends on the active surface area of the used MetNPs, i.e., differences in their active facets and surface energies. Research in this work could make some contributions to this field. The advantage can be seen in the previously mentioned goals and characteristics that our composites (Ag@SBA-15, Au@SBA-15) need to meet. The characteristics/goals are as follows: (a) a low concentration of the active component (Ag and Au), which is lower than in previous studies [34–38], (b) the speed of action—faster than reported similar systems [34–37], and (c) the antimicrobial efficacy under these conditions.

## 2. Materials and Methods

### *2.1. Materials*

The reagent grade materials—silver nitrate ($AgNO_3$, ≥99.0%, CAS Number: 7761-88-8), gold (III) chloride trihydrate ($HAuCl_4 \cdot 3H_2O$, ≥99.9%, CAS Number: 16961-25-4), sodium hydroxide (NaOH, ≥ 97.0%, CAS Number: 1310-73-2), hydrochloric acid (HCl, 37.0%, CAS Number: 7647-01-0), and tetraethoxysilane (TEOS, 98%, CAS Number: 78-10-4), L-histidine ($C_6H_9N_3O_2$ 98.5-101.0%, CAS Number: 71-00-1)—all purchased from Sigma Aldrich (Hamburg, Germany), together with and Pluronic P123 ($EO_{20}PO_{70}O_{20}$, >98%, CAS

Number: 9003-11-6, BASF) were used as received. Milli-Q deionized water with 18.2 MΩ electrical resistivity was used as a solvent.

### *2.2. Preparation of SBA-15 and Nanocomposites*

SBA-15 was first prepared according to our previous works [41,42], where 4.0 g Pluronic P123, as a surfactant, was dissolved in 30 g of distilled water together with 120 g of 2 M HCl solution and stirred for 1.5 h at 35 °C. Then, 8.50 g of TEOS was added dropwise with vigorous stirring at the same temperature for 1.5 h. The mixture was stirred for the next 20 h at 35 °C, then aged for 48 h at 80 °C, and after cooling at room temperature, it was filtered, washed with 600 mL of distilled water, and dried at the same temperature. The step of calcination was performed in flowing air by slowly increasing the temperature to 500 °C during 8 h and heating for 6 h at 500 °C to decompose the triblock copolymer.

For the preparation of nanocomposites Ag@SBA-15 or Au@SBA-15, 0.05 g SBA-15 was first dispersed in NaOH (0.1 M, 20 mL) together with histidine (1 mM) and put on reflux at 80 °C. After 3 h of vigorous stirring, water solutions of $AgNO_3$ or $HAuCl_4$ (0.1 mM) were added dropwise. Color changes in reaction mixtures to yellow for Ag@SBA-15 and dark red for Au@SBA-15 solutions after 24 h indicated the nanocomposites' formation. To produce a third Au-Ag@SBA-15 nanocomposite, in the as-prepared Ag@SBA-15 solution, precursor $HAuCl_4$ (1 mM, the molar ratio Ag:Au = 1:5) and histidine (1 mM), as a reducing agent, were added. After 24 h of stirring and heating on reflux, the violet color of the reaction solution indicated its formation.

### *2.3. Characterization*

Ultraviolet-visible (UV-Vis) absorption spectra of the aqueous solutions of Ag@SBA-15, Au@SBA-15, and Au-Ag@SBA-15 nanocomposites were captured by a TermoScientific Evolution 600 spectrophotometer (Thermo Fisher Scientific, Waltham, MA, USA). Field-emission scanning electron microscopy (FESEM, Zeiss ULTRA plus, Jena, Germany) and transmission electron microscopy (TEM, JEOL-JEM-2100, 200 kV, (JEOL company, Peabody, MA, USA) were used for the determination of the samples' morphology, crystalline structure, and size. For FESEM characterization, the samples were coated with gold (Ag@SBA-15, Au@SBA-15, and Au-Ag@SBA-15) and carbon and platinum (SBA-15). Selected area electron diffraction (SAED) was used to determine the crystal structure of MetNPs. Powdered samples (samples' solutions were dried at 40 °C, and then powdered) were used for FESEM analysis, while the TEM samples were prepared by drop-casting a single drop of the obtained nanocomposites' solutions onto carbon-coated, 300 mesh copper grids, and were allowed to air dry prior to imaging. The ICDD PDF-4+ software was used to plot the ring electron diffraction patterns of Au and Ag reference cards. The distances of spots or rings in SAED patterns, each corresponding to the defined family of atomic planes, were analyzed and measured with Gatan Digital Micrograph 3.5 software. The ICDD PDF-4+ software was used to plot the ring electron diffraction patterns of Au and Ag reference cards. Fourier transform infrared (FTIR) spectra of the nanocomposites' solutions and SBA-15 powder were carried out by Thermo Nicolet Corporation Model 380 FTIR Spectrophotometer with Attenuated Total Reflection (ATR) mode (Thermo Fisher Scientific,Waltham, MA, USA), using this mode for measurements. To study crystalline structure and composition, X-ray diffraction (XRD) patterns of samples were characterized by the Rigaku SmartLab Diffractometer (CuK$\alpha$ radiation source; step size 0.03°, scanning rate: 5 °/min). For zeta potential (ZP) measurement in a Malvern Nano ZS with a 633 nm He-Ne laser, 1 mg of sample was suspended in 1 mL of phosphate-buffered saline and sonicated. Chemical analysis of the samples was performed by X-ray photoelectron spectroscopy (XPS). SPECS System with XP50M X-ray source for Focus 500 and PHOIBOS 100/150 analyzer was employed, operating at 12.5 kV and 250 W. Excitation of the spectra

was performed with monochromatic Al K$\alpha$ radiation (1486.7 eV). Survey spectra were recorded in the range of 0–1200 eV, with constant pass energy of 40 eV, step size 0.5 eV, and dwell time of 0.2 s in the fixed analyzer transmission (FAT) mode. High-resolution spectra of Au 4f, Ag 3d, Si 2p, O 1s, and C 1s peaks were recorded with a constant pass energy of 20 eV, step size of 0.1 eV, and dwell time of 2 s in the FAT mode. The instrument base pressure was ~$2 \times 10^{-9}$ mbar during the experiments. To minimize the effect of charging at samples, an electron flood gun (SPECS FG15/40) was used for charge neutralization, and all peak positions were referenced to C 1s at 284.8 eV. The data was analyzed after Shirley-type background subtraction and by using 2.3.26 of CasaXPS softwarepackage. The specific Brunauer–Emmett–Teller (BET) surface areas of samples were obtained from the nitrogen adsorption experiments measured at −196 °C after degassing the samples below $10^{-6}$ Torr at 200 °C for 2 h using the Surfer Calculation Software version 1.7.0 BETA (Thermo Fisher Scientific, Carlsbad, California, USA). The pore size distribution was estimated by applying the Barrett–Joyner–Halenda (BJH) method to the desorption branch of the isotherm. Details concerning BET analyses and corresponding references are in the Supplementary Materials [43,44].

### *2.4. Antibacterial Assay*

The antibacterial assay of as-prepared samples, in the concentration range of 1–5 ppm, for 2 and 4 h incubation time, was carried out against Gram-negative bacteria *E. coli* (ATCC 25922) and Gram-positive bacteria *S. aureus* (ATCC 25923) by the standard test method ASTM E 2149-01 (ASTM Designation E 2149-01, 2001). The microbial inoculum was prepared in tryptone soy broth (TSB, Torlak, Belgrade, Serbia), supplemented with 0.6% yeast extract (Torlak, Serbia), and left overnight at 37 °C. Afterward, 9 mL of test sterile physiological saline solutions with different nanocomposites' concentrations (1, 2, and 5 ppm) were inoculated with 1 mL of inoculum. After incubation times of 2 and 4 h at 37 °C, 100 μL aliquots of proper dilution in TSB were placed in sterile Petri dishes and incubated at 37 °C for 24 h. Then, the colony-forming units (CFUs) of each dish were determined and compared to control dishes to calculate changes in the cell growth inhibition, represented as a percentage of cell growth reduction ($R$, %), calculated according to the relation

$$R = \frac{C_0 - C}{C_0} \times 100 \quad (1)$$

where $C_0$ is the number of CFUs from the control sample (SBA without MetNPs), and $C$ is the number of CFUs from treated samples.

### *2.5. Statistical Analysis*

Antibacterial assessment was performed in triplicate. The results are presented as means ± standard deviations. Statistical analysis was conducted using OriginPro 9.0 (OriginLab Corporation, Northampton, MA, USA.). Differences between experimental groups were evaluated by one-way analysis of variance (ANOVA), followed by Tukey's test. A confidence level of 95% was considered statistically significant.

## 3. Results and Discussion

### *3.1. Characterizations*

Specific features of SBA-15, like great mesoporous and specific surface area, as well as various pore radii [41,42], motivated us to use them as a kind of highly ordered mesoporous substrate for MetNPs in the application of antimicrobials. In addition, materials such as SBA-15 can provide additional stability to these NPs, allowing them to be incorporated within the pores or adsorbed on their surface. Since the SBA-15 surface and metal

ions have similar charges, repelling one another, in order to establish an interaction between them, the SBA-15 surface was first functionalized with an amine group [45]. In such an interaction, histidine acquires a significant role, owing to the existence of its great affinity toward SBA-15 due to silanol groups present on the silica's surface serving as binding sites, and the mesoporous structure, which allows histidine molecules easy diffusion into the pores [45]. In addition, at higher pH, as in the presented research, when NaOH is used as the surrounding medium (pH ≥ 10), the interaction between silanol groups and histidine is favored [46,47]. Deprotonation of surface silanol groups is followed by the formation of unstable and negatively charged $SiO^-$ groups that will easily interact with positively charged amino groups from L-histidine through electrostatic interactions. There is a formation of outer-sphere complexes, where histidine coordinates to the silica surface. Additionally, a great contribution to histidine's adsorption on the silica surface, at an extremely high pH, is hydrogen bonding between its functional groups and silanol groups [48]. On the other hand, the imidazole ring represents an electron-rich center that easily reduces metal ions $Au^{3+} \rightarrow Au^0$ and $Ag^+ \rightarrow Ag^0$ [30]. This interaction is particularly favored in the alkaline environment, where there is deprotonation of histidine functional groups—amino moieties and carboxyl groups acting together in reducing metal ions to NPs, capping them, and forming stable electrostatic interactions between them, preventing their aggregation [30].

Morphological characteristics of pure, as-synthesized SBA-15 are presented in Figure 1a,b. Its hexagonal mesostructure, with pore diameter around 3 nm, is clearly noticeable in TEM (Figure 1a), while the SAED pattern reveals amorphousness of SBA-15 (Figure 1a, Inset). The morphology of the SBA-15 is consistent with the previously prepared sample of SBA-15 [41,42], showing elongated rod-shaped grains (1 μm in diameter), laterally closely connected and aggregated into wheat-like structures (FESEM image, Figure 1b). The EDX spectrum (Figure 1b, Inset) has determined the presence of Si, C, and O atoms, as building elements of silica.

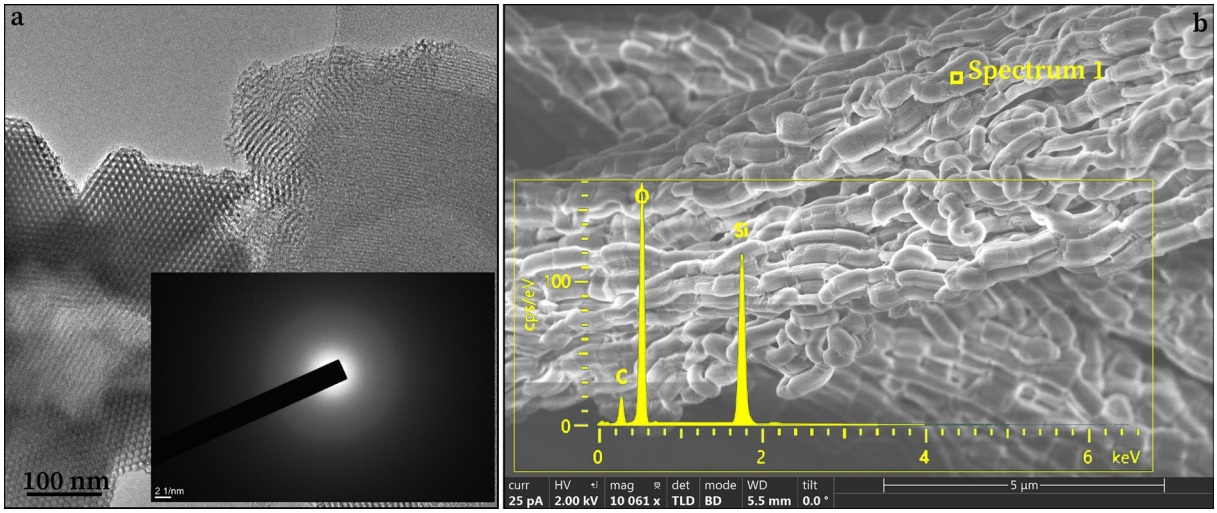


**Figure 1.** TEM (**a**) and FESEM (**b**) images of as-synthesized SBA-15, with corresponding SAED pattern (**a**, **Inset**) and EDX spectrum (**b**, **Inset**).

Concerning AgNPs, AuNPs, and Au-AgNPs, their green synthesis can be successfully achieved by mixing histidine as a reducing/capping material with SBA-15 as a support (Scheme 1). This is first recognized through the color change in the reaction mixtures, and then confirmed by UV-Vis analysis (Figure 2). The surface plasmon resonance (SPR) bands, originating from AgNPs, AuNPs, and Au-AgNPs, are visible at 432, 527, and 503 nm, respectively, similar to the peaks' positions in previous work [49]. Of course, the

presence of SBA-15 and histidine red-shift SPR bands of AgNPs and AuNPs compared to their bands when they are alone in solution [50]. These are surface effects that lead to changes in the optical properties of Ag and AuNPs [51]. This also includes local porosity at the NPs-matrix interface, as the dielectric constant of the matrix (MSPs) is lower than the bulk value in the vicinity of the NP surface [52]. In addition, the SPR peak at 503 nm (Au-Ag@SBA-15) corresponds to particles mostly having Au character, indicating that an undesirable galvanic replacement reaction occurred during synthesis, induced by the electronegativity difference between Ag and Au [53,54]. This means that, due to the higher standard reduction potential of the $AuCl_4^-$/Au (0.99 V, vs. SHE) than that of $Ag^+$/Ag (0.80 V, vs. SHE), AgNPs will be oxidized by $HAuCl_4$, followed by the reduction of $Au^{3+}$ to $Au^0$ according to the following replacement reaction:

$$3Ag_{(s)} + AuCl_4^-{}_{(aq)} \rightarrow Au_{(s)} + 3\,AgCl_{(s)} + Cl^-{}_{(aq)} \quad (2)$$

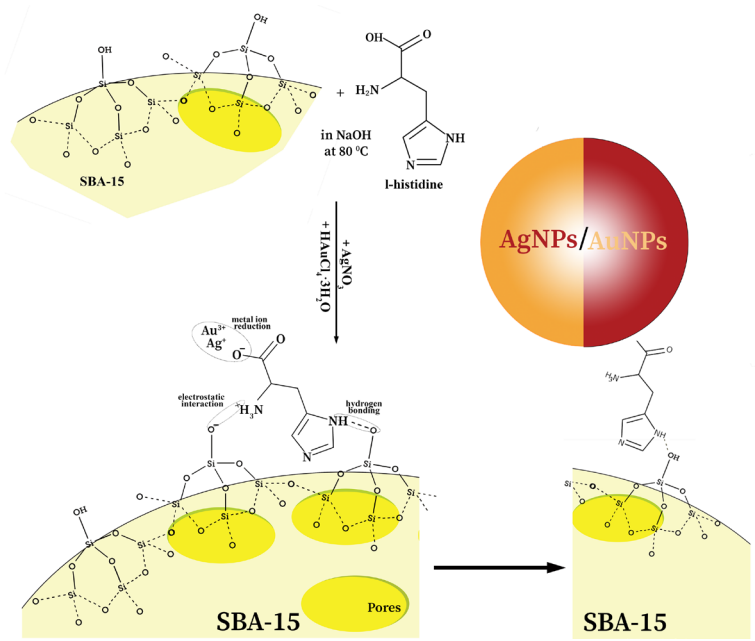


**Scheme 1.** Scheme of synthesis of mesoporous silica (SBA-15) containing Ag, Au, or Au-Ag nanoparticles.

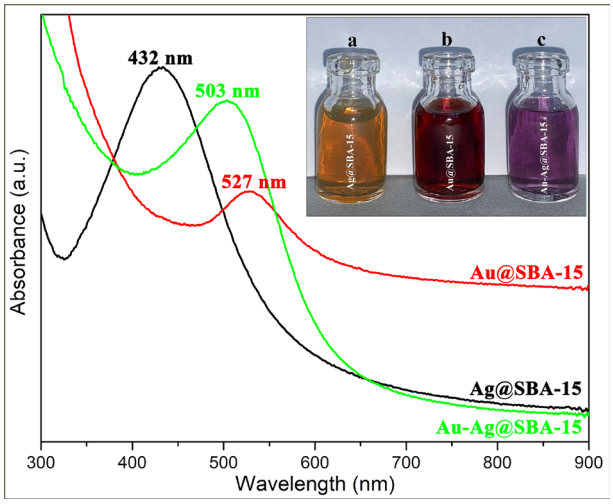


**Figure 2.** UV-Vis spectra of prepared (**a**) Ag@SBA-15, (**b**) Au@SBA-15, and (**c**) Au-Ag@SBA-15 nanocomposites solutions and their colors in the Inset.

This reaction occurs immediately and is faster than the reduction of $Au^{3+}$ by histidine. Since the Au and Ag solids have the same face-centered cubic (fcc) structure with close lattice constants, Au atoms can nucleate and grow on the surface of the Ag, resulting in the formation of Au–Ag alloy NPs. It is important to emphasize that no AgCl precipitate was formed in the solution, as the reaction was carried out around 80 °C, when AgCl is completely soluble in water. Probably, the AgCl nanocrystallites were formed at the site of the reaction and then dissolved into the bulk solvent at this temperature. Also, white solid AgCl precipitate was not observed at the bottom of the container when the reaction mixture was cooled to room temperature, indicating that the silver template had not been completely consumed to reduce $Au^{3+}$ to $Au^{0}$, while a part of the $Au^{3+}$ was reduced by histidine and added to the mixture. Furthermore, the position of the peak at 503 nm of Au-AgNPs was consistent with the plasmon resonance absorption of Ag particles with a gold shell, where their morphology and size are similar to those of the silver templates.

According to the TEM analysis, spherical AgNPs, AuNPs, and bimetal Ag-AuNPs with average diameters of 8.5, 16.0, and 9.0 nm, respectively, were obtained (Figure 3). HRTEM images (Figure 3a,d,g Insets) provide additional information regarding the high level of lattice crystallinity of NPs. The *fcc* lattice structure of AgNPs and AuNPs is confirmed by SAED (Figure 3c,f,i), which are indexed according to the reference cards No. 00-004-0783 for Ag, and No. 00-004-0784 for Au. We have identified very similar lattice constant values of 2.38, 2.31, and 2.35 Å of the (111) planes of Ag, Au, and bimetal NPs, respectively [55]. These results indicate that during the 24 h of stirring and heating on reflux, the gold shells can reconstruct their walls into crystalline structures via Ostwald ripening and form Ag-AuNPs.

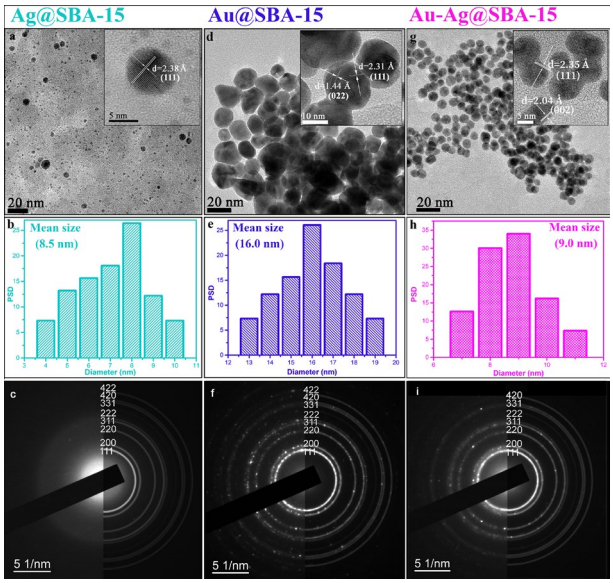


**Figure 3.** TEM with HRTEM (Insets) images (a,d,g), particle size distribution (PSD, b,e,h), and SAED images (c,f,i) of Ag@SBA-15, Au@SBA-15, and Au-Ag@SBA-15.

It is important to note that the hexagonal mesostructure of SBA-15 is not visible in the TEM images of the nanocomposites, and subsequent BET analysis was performed to see if its changes occurred after supporting Ag, Au, or Au-Ag NPs. Based on the BET analysis, surface parameters such as the surface area, mean pore diameter, and total pore volume of pure SBA-15 and nanocomposites were revealed.

As can be seen from the nitrogen adsorption–desorption isotherms of powdered samples, presented at Figure 4, the isotherm of pure SBA-15 (Figure 3a) corresponds to a Type IV isotherm with an H1 hysteresis loop, indicating the presence of a mesoporous

structure, while according to the IUPAC classification [56], isotherms of nanocomposites Ag@SBA-15, Au@SBA-15, and Au-Ag@SBA-15 (Figure 4b–d) are type III, which indicates weak adsorbate–adsorbent interactions [57]. The Type IV profile is characteristic of capillary condensation within mesopores, while the well-defined H1 hysteresis loop suggests a narrow pore size distribution and the presence of cylindrical or uniform mesopores with open ends. Such features are typically associated with ordered pore structures, which are favorable for applications involving diffusion and adsorption of larger molecules. Furthermore, the specific surface area calculated by the BET equation, median pore radius, and cumulative pore volume of the samples (presented in Table S1 in Supplementary Materials) suggest a decrease in the specific surface area (from 675 $m^2/g$ for pure SBA-15 to even 3 $m^2/g$ for the Ag@SBA-15 nanocomposite). Such a large decrease in specific surface area indicates that the formed MetNPs have deposited not only on the surface of the silica but also inside the pores. The nanoparticles probably blocked the internal surface that, in this case, nitrogen molecules could access during adsorption measurements, which further led to a lower measured surface area [58]. In addition, measured median pore diameters (Supplementary Materials, Table S1) indicated an increase when MetNPs are incorporated into SBA-15. As some researchers suggested, when MetNPs are larger than the initial pore size, they can act as a lump that will push the pore walls, and consequently expand the pore and/or reshape the pore into a larger one [59]. In other words, incorporated MetNPs reduce accessibility of the pore surface, eliminating smaller pores from the distribution, which further leads to the shifting of the median pore size to higher values. Considering the size distribution of the formed Ag and AuNPs (PSD: Figure 3b,e,h), their average diameter values are larger than the pore size of the SBA-15 (around 3 nm), so these nanoparticles will be adsorbed on its surface, while the smaller ones could be incorporated into the pores. These results are in agreement with the results gained from the BET analysis.

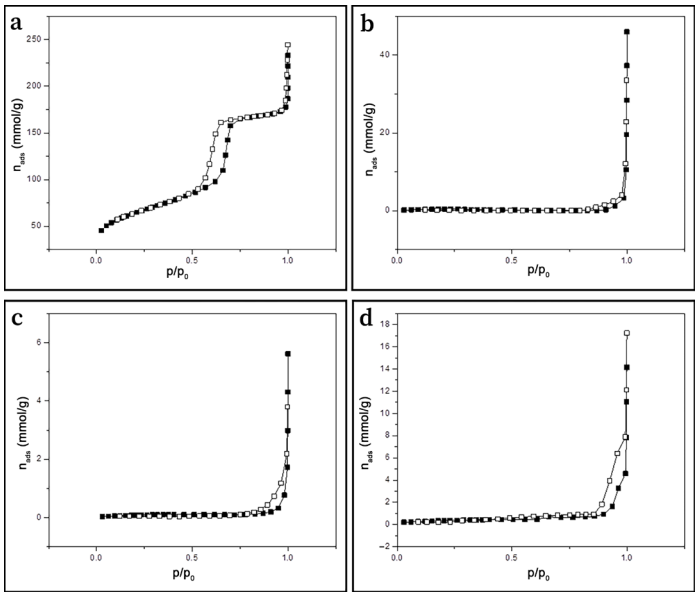


**Figure 4.** Nitrogen adsorption isotherms, as the amount of $N_2$ adsorbed as a function of relative pressure for powdered SBA-15 (**a**), Ag@SBA-15 (**b**), Au@SBA-15 (**c**), and Au-Ag@SBA-15 (**d**). Solid (black) symbols—adsorption, open (white) symbols—desorption.

Characterization of the morphology of prepared samples indicated that SBA-15 has the same granular form in all nanocomposites (Ag@SBA-15, Au@SBA-15, and Au-Ag@SBA-15), which is used as a platform/matrix for them (Figure 5a–c). It was evident from the elemental composition study (EDX) that Ag@SBA-15 and Au@SBA-15

nanocomposites showed the presence of silica and oxygen from SBA-15 and Ag from AgNPs or Au from AuNPs (Figure 5a,b). In addition, the EDX spectrum of the Au-Ag@SBA-15 nanocomposite confirms the presence of both NPs (Ag and Au) in its spectral signal, shown in Figure 5c.

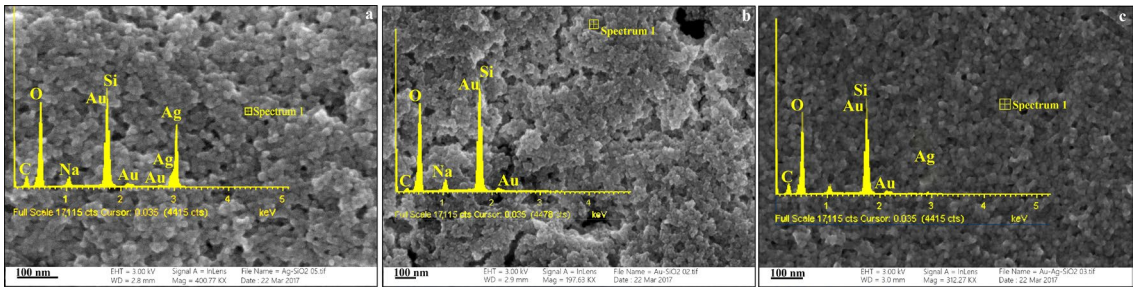


**Figure 5.** FESEM images of (**a**) Ag@SBA-15, (**b**) Au@SBA-15, and (**c**) Ag@SBA-15 nanocomposites with their EDX spectra.

The absolute value of the zeta-potential of histidine functionalized SBA-15 in phosphate-buffered saline (PBS) showed a slight increase compared to Ag@SBA-15, Au@SBA-15, and Au-Ag@SBA-15, from −30.2 mV to −24.5, −25.1, and −24.3 mV, respectively. The presence of the deprotonated carboxyl group ($–COO^-$) of histidine (imidazole part is unprotonated) at higher pH makes the surface of MetNPs negatively charged, and consequently, the repulsive electrostatic force of inter-particle led to the preclusion of their aggregation. The TEM analysis confirmed that MetNPs did not agglomerate and were separated.

According to XRD analysis of samples, four distinct diffractions peaks are visible at 2θ ~ 38.2°, 44.3°, 64.7°, and 77.8° corresponding to (111), (200), (220), and (311) planes, respectively, of both nanocrystalline Ag [JCPDS file number: 04-0783] and Au [JCPDS file number: 04-0784] in Ag@SBA-15 and Au@SBA-15 nanocomposites (Figure 6) [60]. This confirms their similar fcc crystal structure, which was also observed on HRTEM and SAED. The strongest peak at 2θ~38.2° observed in both nanocomposites (Ag@SBA-15 and Au@SBA-15) revealed the predominant growth of Ag and Au in the direction of the (111) plane and good crystallinity (also confirmed by SAED). These inherent peaks, although of much lower intensity compared to the aforementioned one, are also observable in the diffractogram of the third nanocomposite (Au-Ag@SBA-15), corroborating that a galvanic replacement reaction occurred between Ag and Au. Furthermore, in the Ag@SBA-15 and Au-Ag@SBA-15 diffractograms, there are noticeable peaks originating from the oxidized part of the AgNPs at 28.9°, 32.2°, 33.8°, 55.2°, and 57.8°, corresponding to (100), (110), (111), and (211) planes, respectively [61]. Taking into account that some AgNPs with a size < 3 nm are dispersed within the pores of a mesoporous silica, they exhibit a certain amount of free surface (interface towards the pore walls) being in contact with ambient air, since the pores are interconnected and open [62,63]. These AgNPs are chemically highly surface active due to their small size and oxidize in contact with oxygen in the air. In contrast to AgNPs, AuNPs are inert towards most molecules, e.g., oxygen does not adsorb on the Au (110) and (111) surfaces, and the aforementioned peaks do not exist in the Au@SBA-15 nanocomposite. In addition, this could also be an aftermath of the effect of the galvanic replacement reaction, when AgNPs will be oxidized by $HAuCl_4$. On the other hand, the amorphous nature of SBA-15 visible from the SAED pattern (Figure 1a, Inset) was confirmed as well—the XRD pattern of SBA-15 exhibits a single, very broad peak at 2θ ~ 23°, as characteristic of the amorphous silica framework (Figure 6, Inset) [18]. The intensity of this peak in all nanocomposites is hardly visible due to its low diffraction signals compared to diffraction from both metals.

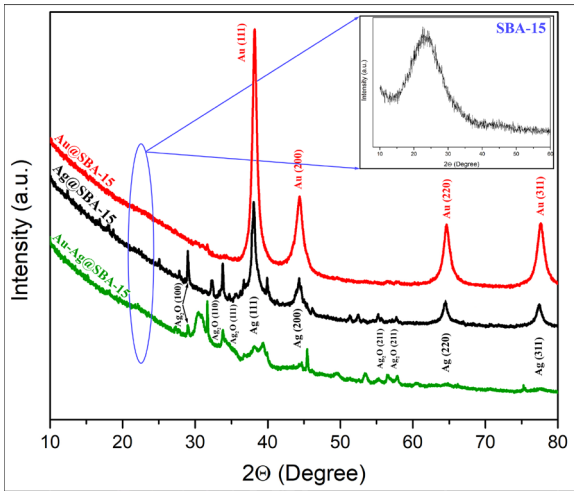


**Figure 6.** XRD patterns of Ag@SBA-15, Au@SBA-15, and Au-Ag@SBA-15 nanocomposites. Inset: XRD patterns of SBA-15.

Furthermore, basic structural characteristics (cell parameters) and microstructural parameters (crystallite size and microstrain) based on the broadening of the diffraction peaks of Ag@SBA-15 and Au@SBA-15 nanocomposites were calculated from the presented XRD patterns. The XRD patterns were refined by the whole-pattern decomposition procedure (Le Bail fitting) using the FullProf software package (Version 1.9c), considering the instrumental peak broadening [64,65]. The applied analysis included refining all four characteristic peaks originating from a *fcc* lattice (S.G. Fm-3m): (111), (200), (220), and (311). The values of lattice parameters *a* were determined to be 4.08732(9) Å and 4.07870(5) Å for Ag@SBA-15 and Au@SBA-15, respectively. The formed nanocomposites Ag@SBA-15 and Au@SBA-15 consist of crystallites that are calculated to be nano-sized on the order of 9 nm and have a small amount of microstrain, 0.05%, which represents the overall crystal imperfections (lattice strain and defects like dislocations and point defects).

The SBA-15/histidine interaction, metal ions' reduction by histidine, and nanoparticles' formation were confirmed by FTIR analysis (Figure 7). Some of the histidine characteristic bands at ≈1490 and 1405 $cm^{-1}$, corresponding to amino moieties and carboxyl groups, respectively, are shifted to lower wavenumbers 1460 and 1370 $cm^{-1}$, indicating an interaction between histidine and Ag or AuNPs. It denotes a capping role of histidine with MetNPs through the amino and carboxyl groups [30]. Furthermore, vibrations characteristic for SBA-15 are shifted and/or less intense/disappeared compared to pure SBA-15 (Figure 7, Inset), from 3456 (Si—OH stretching vibrations), 1636 (—C═O stretching vibration), and 1082 $cm^{-1}$ (asymmetric stretching vibrations of the Si—O—Si) to 3400, 1627 and 1060 $cm^{-1}$, respectively, suggesting interactions with histidine and MetNPs [41]. Moreover, the significant reduction in band intensity at 1060 $cm^{-1}$ (Si—O—Si) observed for all the nanocomposite samples confirmed interaction between histidine and —$SiO_2$ moieties, i.e., successful functionalization of mesoporous silica by amine group from histidine. It also confirmed changes in the pore structure after nanoparticles' adsorption, i.e., reducing the specific surface area of pure SBA-15, which may be due to inherent disorder in the structure of the silica.

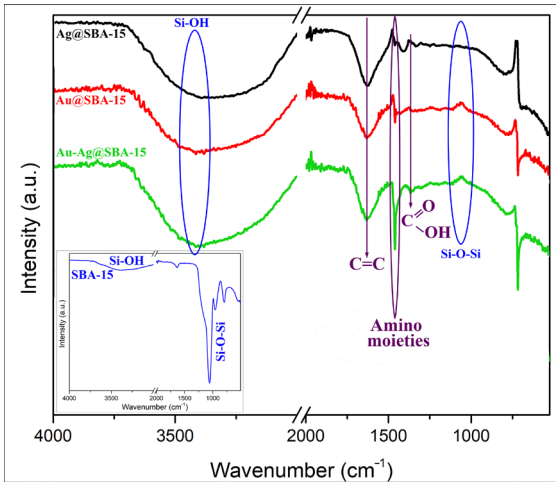


**Figure 7.** FTIR spectra of Ag@SBA-15, Au@SBA-15, and Au-Ag@SBA-15 nanocomposites. Inset: FTIR spectrum of SBA-15.

In addition, in order to analyze the surface elemental composition and chemical environment of the synthesized SBA-15 and Ag@SBA-15, Au@SBA-15, and Au-Ag@SBA-15 nanocomposites, XPS analysis was employed. The survey spectra of pure SBA, as well as Au- and Ag-loaded SBA systems, are presented in Figure 8a–l. They reveal the presence of silicon, carbon, oxygen, gold, and silver as the main elements. Additionally, other species originating from the precursors used during material synthesis, such as Na, Cl, and N, are also detected. Quantitative analysis shows a Au 4f and Ag 3d atomic concentration of 0.3 at% in both cases of modified SBA with single ions, whereas with the sample containing both Au and Ag ions, XPS only detected a weak signal of gold species.

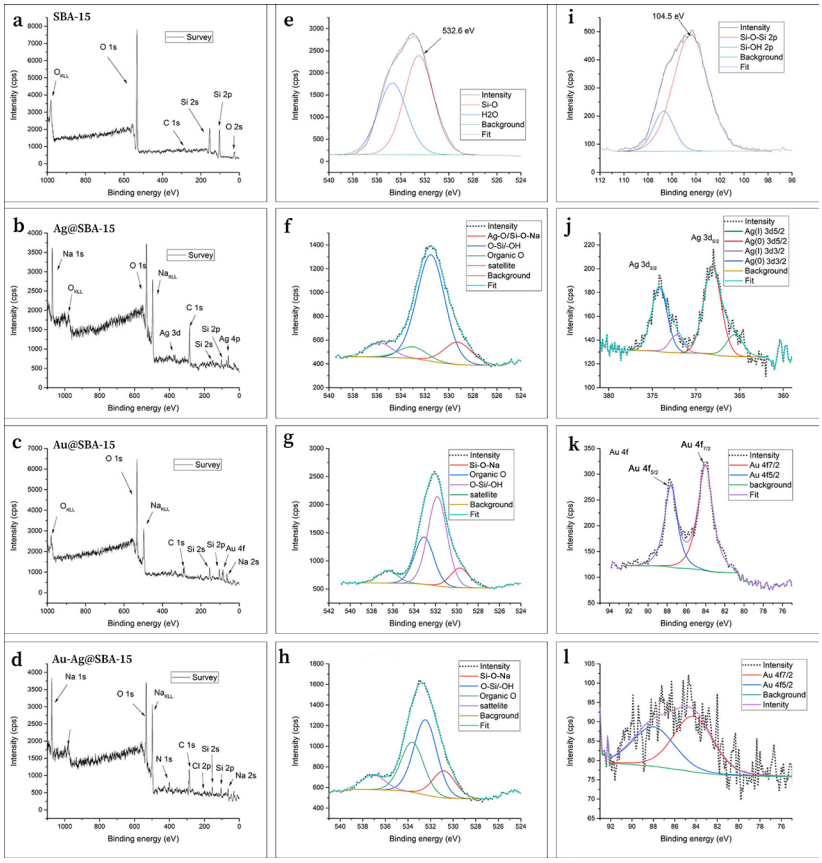


**Figure 8.** XPS spectra of pure SBA-15 (**a**,**e**,**i**) and Ag@SBA-15 (**b**,**f**,**j**), as well as Au@SBA-15 (**c**,**g**,**k**) and Au-Ag@SBA-15 (**d**,**h**,**l**) nanocomposites.

The O 1s high-resolution spectra of all samples (Figures 8e–h) consistently show a dominant peak around 532.6 eV corresponding to the siloxane (Si–O–Si) network in the silica framework, accompanied by contributions of Si-O-Na at 530 eV, Ag-O bond at the same energy, organic O at around 533 eV, and adsorbed water. These features confirm the preserved mesoporous silica structure in both pristine SBA-15 and metal-modified samples, with subtle shifts attributed to metal-induced changes in the local oxygen environment [66]. Confirmation for silicate formation upon metal loading is observed in the Si 2p region. For pristine SBA-15, the Si 2p spectrum shows the Si–O–Si ($Si^{4+}$) component at ~104.5 eV, with a weaker Si–OH contribution at slightly higher binding energy (Figure 8i). In contrast, all loaded systems (Figure S2) do not exhibit an −OH contribution, but instead show an additional lower-binding-energy component at ~103 eV, attributable to silicates, in this case sodium silicate species (Si–O–Na).

Regarding the metal species, the XPS analysis reveals distinct features of silver and gold in the nanocomposites. In the Ag@SBA-15 nanocomposite (Figure 8j), the Ag 3d spectrum shows characteristic spin–orbit split peaks of Ag 3d5/2 and 3d3/2 at 368.2 and 374.2 eV, which is consistent with predominantly metallic silver ($Ag^0$) along with minor oxidized species detected at lower binding energies [67]. In the Au@SBA-15 nanocomposite (Figure 8k), the Au 4f spectrum exhibits the spin–orbit doublet peaks at 84 and 87.7 eV separated by 3.7 eV, typical for metallic gold nanoparticles, with slight binding energy shifts indicating interaction with the silica support [67]. Notably, in the Au-Ag@SBA-15 nanocomposite (Figure 8l), only weak Au 4f signals are detected, confirming the exclusive detection of metallic gold species, while silver peaks are absent or below the detection limit. These observations imply successful incorporation and reduction in metal nanoparticles within the SBA-15 matrix, with the oxygen spectra also reflecting subtle modifications due to metal-support interactions.

### *3.2. Antibacterial Efficacy of Nanocomposites*

The results of the quantitative antibacterial efficiency of Ag@SBA-15, Au@SBA-15, and Au-Ag@SBA-15 nanocomposites were determined over 2 and 4 h exposure time with pathogenic bacteria *E. coli* and *S. aureus* (see Figure 9, details are given in Supplementary Materials, as Tables S2 and S3). As derived from Tables S2 and S3, even 1 ppm of active component in Ag@SBA-15 reached an excellent bactericidal value of 99.99% after very fast (2 h) interaction with both strains. This concentration is enough for the number of *Escherichia* colonies to be less than 10 after 2 h, the same as the number of *Staphylococcus* colonies after 4 h. The difference in time activities between the two strains could be attributed to the fact that *E. coli* possesses a thinner cell wall, which might make them more susceptible to Ag ion penetration. Unlike the previous nanocomposite, 5 ppm of Au@SBA-15 reached an acceptable value of 99.98% after 4 h exposure to *E. coli*, and demonstrated a somewhat weaker reducing ability of 94.71% toward *S. aureus* at the same time. In both nanocomposites, a higher surface area to volume ratio of nanoparticles enables the acceleration of metal ion release. In addition, it is expected that the effectiveness of Ag@SBA-15 is higher than Au@SBA-15 as the AgNPs are a stronger antibacterial agent than AuNPs; their small size and active (111) planes at the surface, as well as SBA-15's advantages as the support matrix, wherein a large area of contact with microbes physically surrounds them, has high negative zeta potential and effective high local concentration of the NPs adsorbed on its surface and in pores, which give fast and great contribution to bacterial growth inactivation and final death. Moreover, the AgNPs are considered the best alternative to antibiotics, as they have great toxic effects against a wide range of pathogenic organisms without the addition of other compounds. These NPs also act as a source that releases silver ions, which represent the active antimicrobial principle. It is worth noting that, because a functional biofilm protects bacteria from all silver species (AgNPs, $Ag_2O$, and Ag ions) by

reducing their mobility through it, and also because highly charged NPs would have problems diffusing due to strong electrostatic interactions with biofilms, the best antibacterial effects are usually obtained when Ag ions, as directly toxic species, are released [68]. Furthermore, AgNPs generate reactive oxygen species (ROS) in the shape of superoxide and hydroxyl radicals, contributing to their antibacterial activity, through penetrating membranes and causing damage more effectively than singlet oxygen produced as the primary ROS by AuNPs [69]. Lower antibacterial activity of Au@SBA-15 nanocomposite compared to Ag@SBA-15 may also be associated with gold being more biologically inert relative to silver [70]. It can disrupt the bacterial cell wall, causing leakage of intracellular components, but to a lesser extent compared to silver [71]. Nevertheless, the results of this study demonstrate that both nanocomposites, Ag@SBA-15 and Au@SBA-15, due to the synergetic effect of SBA-15 and MetNPs, are capable of sensitizing the tested resistant strains through establishing interactions with their membranes and facilitating cell wall loosening and degradation. Moreover, their high efficacy allows them to affect multiple novel bactericidal pathways that they evolve to survive. According to our previous work with a nanocomposite based on MetNPs and the literature data of different authors, their cellular mechanism for antibacterial activity also shows a cascade of events that leads to a disturbance in homeostasis, generation of toxic free radicals, oxidative stress, interference with respiration, leakage of nucleic acids, enzymes' deactivation, and ultimately, cell death [24,34,72–75].

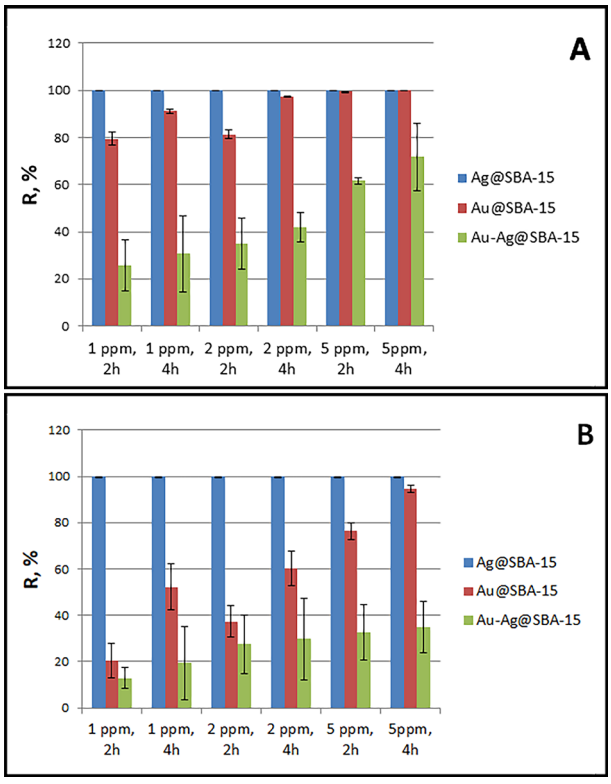


**Figure 9.** Concentration-dependent reduction ability (R, %) of the Ag@SBA-15, Au@SBA-15, and Au-Ag@SBA-15 on *E. coli* (**A**) and *S. aureus* (**B**), over 2 and 4 h incubation time. Data are presented as mean ± standard deviation ($n$ = 3).

Noticeably, the effective Ag concentration of 1 μg/mL (1 ppm) in our study is significantly lower than demonstrated in similar systems of Ag–mesoporous silica published previously (Table 1) [34–38]. For example, Liong et al. used 20–100 μg/mL of Ag@mesoporous silica with AgNPs of 20 nm in size against *E. coli* [35]. The formation of colonies was fully inhibited when the LB-agar plates contained 100 μg/mL of the particles. In

another study, authors used small Ag nanoclusters 2 nm in size to decorate mesoporous silica against *S. aureus* and showed that 5 μg/mL Ag reached a killing efficacy of 99.99% after 12 h [34]. In the antibacterial test for *E. coli*, Joardar et al. presented AgNPs (15–18 nm in size)—mesoporous silica nanocomposites that exhibited cell growth reduction of 95% after 24 h of incubation with Ag content of 6.1 μg/mL [36]. In the case of AuNPs, Lodeiro et al. explored the application of Au nanorods (with a length of 42.4 ± 9.0 nm and a width of 19.2 ± 3.8 nm) as photothermal agents coated with a mesoporous silica shell (AuNRs@Simes) and loaded with methylene blue as a model drug for potent antimicrobial activity against *E. coli* and *S. aureus* bacteria [37]. They showed that after laser irradiation during a short time period, this system (1.0 mg/mL) had a pronounced antibacterial activity (~8 log10 unit reduction) against *E. coli* and *S. aureus*. Some other examples of the antibacterial activity of Ag–silica or Au–silica nanocomposites against both strains and their characteristics compared to the activity of samples in this work (Ag@SBA-15 and Au@SBA-15) are shown in Table 1. It can be concluded that some key advantages of our nanocomposites are the small diameter of both NPs, which results in a large surface area for contact with microbes, and low concentration of AgNPs or AuNPs in nanocomposites, but effective high local concentration of these NPs adsorbed on silica surface, which results in high antimicrobial efficiency and further shortening the incubation time. However, it should be noticed that although there is a large number of studies on MetNPs–mesoporous systems with high antimicrobial properties, their efficacy varies depending on the type of MetNPs, their size, shape, concentration, and surface chemistry, as well as the surface chemistry of silica particles and the methods used to assess antibacterial efficacy. Therefore, sometimes it is difficult to correlate or compare data from different studies to establish product quality attributes.

**Table 1.** Comparison of various Ag– or Au–mesoporous silica nanocomposite activity toward *E. coli* and *S. aureus*.

| Nanocomposites of Ag– or AuNPs—Mesoporous Silica | Preparation Method; Size (nm), Shape, and $\lambda_{max}$ of Ag or AuNPs | Ag or Au Concentration (μg/mL) | Strain | Microbial Reduction (R, %), Time of Incubation (h) |
|---|---|---|---|---|
| Ag–mesoporous silica | Prepared AgNPs (20 nm spheres, 425 nm) by boiling solution of $Ag^+$, oleylamine, and toluene under nitrogen. These were used as the seed for the growth of silica. | 20–100 | *E. coli* | 100 μg/mL fully inhibited colonies [35]. |
| Ag–mesoporous silica | Prepared AgNPs (2 nm nanoclusters, 481 nm) by reduction of $AgNO_3$ with $NaBH_4$. These were used with Stober method to synthesize nanocomposite. | 5.0 | *S. aureus* | 99.99% after 12 h [34]. |
| Ag–mesoporous silica | In situ synthesis of AgNPs (15–18 nm in size) and silica particles by cetyltrimethylammonium perchlorate and TEOS. | 6.1 | | 95% after 24 h [36]. |
| Au–mesoporous silica | Synthesis of Au nanorods (length 42.4 ± 9.0 nm, width 19.2 ± 3.8 nm, 518 and 656 nm) coated with a mesoporous silica | $1.0 \times 10^3$ | *E. coli*, *S. aureus* | ~8 log10 unit reduction against both strains after laser irradiation during a short time period [37]. |

| | | | | |
|---|---|---|---|---|
| | shell and conjugated with methylene blue. | | | |
| Ag–mesoporous silica | In situ synthesis silica and AgNPs (2–10 nm spheres) by co-condensation method in dilute sodium hydroxide solution (Cai reaction). | 3.36<br>13.44 | *E. coli*,<br>*S. aureus* | 99.99% of *E. coli* was killed by the first 2 h;<br>99.99% of *S. aureus* was killed in the first 2 h [38]. |
| Ag–mesoporous silica,<br>Au–mesoporous silica | In situ synthesis of AgNPs (8.5 nm spheres, 432 nm) and AuNPs (16 nm spheres, 527 nm) in the prepared silica solution by Pluronic P123 and TEOS. | 1<br>5 | *E. coli*,<br>*S. aureus* | 99.99% reduction in both strains after 2 h;<br>99.98% *E. coli* and 94.71 % *S. aureus*, after 4 h [This study]. |

Unlike the activity of previously tested nanocomposites (Ag@SBA-15, Au@SBA-15), the antimicrobial role of Au-Ag@SBA-15 toward both pathogens is different and affected by the galvanic replacement reaction between the two metals and their distribution inside the particles. Nevertheless, it has been shown that its reduction ability against *E. coli* is 71.65% after 4 h at a concentration of 5 ppm. Although the complete growth inhibition was not achieved, the reduction in viable cell number was significant ($p < 0.05$). Under the same conditions, increasing the concentration and time of exposure had no effect against *S. aureus*, suggesting an inability of this system to completely inhibit their growth (Table S2 and S3). This means that some Ag remains, i.e., the silver template has not been completely consumed to reduce $Au^{3+}$ to $Au^{0}$, which affects the potential antibacterial properties of the material. In this structure, the surface condition of the outer metal is influenced by the function of the inner metal surface, which changes the antibacterial activity of Au-Ag@SBA-15 to lower values and slows down the whole process. Furthermore, *S. aureus*, due to a thicker peptidoglycan cell wall layer, requires higher Au-Ag@SBA-15 concentrations and/or longer time to inhibit the growth when compared to *E. coli*, and to achieve better activity of this nanocomposite.

## 4. Conclusions

Presented nanocomposites of MetNPs and SBA-15, synthesized by the "green" method, demonstrated interesting physicochemical characteristics. Prepared SBA-15, as support for MetNPs, has a hexagonal mesostructure, with a pore diameter of around 3 nm. It was shown that the incorporation of MetNPs throughout its matrix not only changes the chemical characteristics of its surface, but also the physical ones—the specific surface area of SBA-15 decreases due to filling the pores with nanoparticles that can act as a lump, pushing the pore walls, and consequently increasing the median pore radius. Nevertheless, it was found that the antimicrobial activity of the nanocomposites is more than satisfying. Unlike the Ag@SBA-15 nanocomposite, which has excellent antibacterial activity against *E. coli* and *S. aureus*, at a very low concentration (1 ppm) and incubation time (2 h), Au@SBA-15 has good activity, only at a higher concentration and incubation time (5 ppm, 4 h). Such activity of both nanocomposites is due to the large specific surface area, negative zeta potential, and high local concentration of the NPs adsorbed on the SBA-15 surface and in pores. It enables a large contact area with microbes, physically surrounding them, giving a fast and great contribution to bacterial growth inactivation and final death. Their synergistic effect has an impact on the resulting antibacterial efficacy, enabling them to target multiple new bactericidal pathways that they develop in their defense. Considering their activity, it could be expected that their alloy structure supported on SBA-15 would have improved efficacy. However, the Au-Ag@SBA-15 nanocomposite did not show as outstanding a performance as those of its counterparts, being

only able to slightly reduce *S. aureus* growth in contrast to *E. coli*, when it achieved a reduction of 91.19%. It is limited by the galvanic replacement reaction between two metals that occurred during the synthesis of the nanocomposite, where most of the Ag template was consumed to reduce Au ions instead of histidine, which drastically slowed down the antibacterial activity of Au-Ag@SBA-15. Nevertheless, "green" methodology and low active component concentration in the Ag@SBA-15 (1 ppm) nanocomposite, and even 5 ppm of Au@SBA-15 nanocomposite, with good antibacterial features, allow for utilization in wastewater disinfection, and there is always room for additional feature enhancement in order to achieve greater activity with even shorter contact times. Their application provides a potential substitute for existing bacterial disinfectants and can be used as a starting point for investigating innovative materials in this area.

**Supplementary Materials:** The following supporting information can be downloaded at: https://www.mdpi.com/article/10.3390/technologies13100458/s1, Figure S1: Pore size distribution of SBA-15 (a), Ag@SBA-15 (b), Au@SBA-15 (c), and Au-Ag@SBA-15 (d); Figure S2: High resolution spectra of Si 2p region for Au loaded SBA-15 system. Table S1: Porous properties of SBA-15, Ag@SBA-15, Au@SBA-15, and Au-Ag@SBA-15; Table S2: Antibacterial efficacy of Ag@SBA-15, Au@SBA-15, and Au-Ag@SBA-15 nanocomposites after 2 and 4 h incubation time with E. *coli*; Table S3: Antibacterial efficacy of Ag@SBA-15, Au@SBA-15, and Au-Ag@SBA-15 nanocomposites after 2 and 4 h incubation time with *S. aureus*.

**Author Contributions:** Conceptualization, U.S. and V.V.; methodology, U.S.; formal analysis, U.S., M.K. and V.V.; investigation, U.S., D.M., M.K., S.D., S.Š., M.O., T.B., D.P., and T.M.A.; data curation, U.S. and V.V.; writing—original draft preparation, U.S.; writing—review and editing, M.K. and V.V.; supervision, V.V. All authors have read and agreed to the published version of the manuscript.

**Funding:** This research was funded by the Ministry of Science, Technological Development and Innovation of the Republic of Serbia (contract no. 451-03-136/2025-03/200017).

**Institutional Review Board Statement:** Not applicable.

**Informed Consent Statement:** Not applicable.

**Data Availability Statement:** Data will be available on request.

**Acknowledgments:** The authors express their gratitude to the Ministry of Science, Technological Development, and Innovation of the Republic of Serbia for the financial support (contract no. 451-03-136/2025-03/200017). M.O. acknowledges the Slovenian research and innovation agency, core funding P2-0105.

**Conflicts of Interest:** The funders had no role in the design of the study; in the collection, analyses, or interpretation of data; in the writing of the manuscript; or in the decision to publish the results.

## Abbreviations

The following abbreviations are used in this manuscript:

| | |
|---|---|
| UV-Vis | Ultraviolet-Visible |
| TEM | Transmission Electron Microscopy |
| HRTEM | High-Resolution Transmission Electron Microscopy |
| SAED | Selected Area Electron Diffraction |
| FESEM | Field-Emission Scanning Electron Microscopy |
| XRD | X-Ray Diffraction |
| FTIR | Fourier Transform Infrared |
| XPS | X-ray Photoelectron Spectroscopy |
| BET | Brunauer–Emmett–Teller |

| | |
|---|---|
| MSPs | Mesoporous Silica Particles |
| MetNPs | Metal Nanoparticles |
| TSB | Tryptone Soy Broth |
| LB | Luria–Bertani |
| CFUs | Colony Counting Units |
| SPR | Surface Plasmon Resonance |
| fcc | Face-Centered Cubic |
| PSD | Particle Size Distribution |

## References


1. MacGowan, A.; Macnaughton, E. Antibiotic resistance. *Medicine* **2017**, *45*, 622–628.
2. Turner, N.A.; Sharma-Kuinkel, B.K.; Maskarinec, S.A.; Eichenberger, E.T.; Shah, P.P.; Carugati, M.M.; Holland, T.L.; Fowler, V.G. Methicillin-resistant Staphylococcus aureus: An overview of basic and clinical research. *Nat. Rev. Microbiol.* **2019**, *17*, 203–218.
3. Biswas, S.; Bal, M.; Pati, S.; Rana, R.; Dixit, S.; Ranjit, M. Antibiotic resistance in toxigenic E. coli: A severe threat to global health. *Discov. Med.* **2024**, *1*, 72.
4. Davis, M.; Whittaker, A.; Lindgren, M.; Djerf-Pierre, M.; Manderson, L.; Flowers, P. Understanding media publics and the antimicrobial resistance crisis. *Glob. Public Health* **2018**, *13*, 1158–1168.
5. Vodnik, V.; Stamenović, U.; Vukoje, I. Nanocomposites of metal nanoparticles and polymer as platform of alternative approach in combating antimicrobial resistance. In *Nanotechnology Based Strategies for Combating Antimicrobial Resistance*; Wani, I.A., Wani, M.Y., Rai, A., Eds.; Springer Nature: Singapore, 2024; Chapter 18, pp. 489–510.
6. Beyth, N.; Houri-Haddad, Y.; Domb, A.; Khan, W.; Hazan, R. Alternative antimicrobial approach: Nano-antimicrobial materials. *Evid. Based Complement. Altern. Med.* **2015**, *2015*, 246012.
7. Zhao, X.; Tang, H.; Jiang, X. Deploying gold nanomaterials in combating multi-drug-resistant bacteria. *ACS Nano* **2022**, *16*, 10066–10087.
8. Bernardos, A.; Piacenza, E.; Sancenón, F.; Hamidi, M.; Maleki, A.; Turner, R.J.; Martínez-Máñez, R. Mesoporous silica-based materials with bactericidal properties. *Small* **2019**, *15*, e1900669.
9. Zhu, Y.; Xu, J.; Wang, Y.; Chen, C.; Gu, H.; Chai, Y.; Wang, Y. Silver nanoparticles-decorated and mesoporous silica coated single-walled carbon nanotubes with an enhanced antibacterial activity for killing drug-resistant bacteria. *Nano Res.* **2020**, *13*, 389–400.
10. Wang, L.; He, H.; Zhang, C.; Sun, L.; Liu, S.; Yue, R. Excellent antimicrobial properties of silver-loaded mesoporous silica SBA-15. *J. Appl. Microbiol.* **2014**, *116*, 1106–1118.
11. Kankala, R.K.; Lin, W.Z.; Lee, C.H. Combating antibiotic resistance through the synergistic effects of mesoporous silica-based hierarchical nanocomposites. *Nanomaterials* **2020**, *10*, 597.
12. Deng, Y.; Wei, J.; Sun, Z.; Zhao, D. Large-pore ordered mesoporous materials templated from non-Pluronic amphiphilic block copolymers. *Chem. Soc. Rev.* **2013**, *42*, 4054.
13. Martínez-Carmona, M.; Gun'ko, Y.; Vallet-Regí, M. Mesoporous silica materials as drug delivery: "The Nightmare" of bacterial infection. *Pharmaceutics* **2018**, *10*, 279.
14. Şen Karaman, D.; Manner, S.; Rosenholm, J.M. Mesoporous silica nanoparticles as diagnostic and therapeutic tools: How can they combat bacterial infection? *Ther. Deliv.* **2018**, *9*, 241–244.
15. Chen, Y.; Chen, H.; Shi, J. In vivo bio-safety evaluations and diagnostic/therapeutic applications of chemically designed mesoporous silica nanoparticles. *Adv. Mater.* **2013**, *25*, 3144–3176.
16. Wang, Y.; Zhao, Q.; Han, N.; Bai, L.; Li, J.; Liu, J.; Che, E.; Hu, L.; Zhang, Q.; Jiang, T.; et al. Mesoporous silica nanoparticles in drug delivery and biomedical applications. *Nanomed. Nanotechnol. Biol. Med.* **2015**, *11*, 313–327.
17. Liong, M.; Lu, J.; Kovochich, M.; Xia, T.; Ruehm, S.G.; Nel, A.E.; Tamanoi, F.; Zink, J.I. Multifunctional inorganic nanoparticles for imaging, targeting, and drug delivery. *ACS Nano* **2008**, *2*, 889–896.
18. Kanti, S.K.; Chaudhary, P.; Han, S.S. Environmentally sustainable route to $SiO_2$@Au–Ag nanocomposites for biomedical and catalytic applications. *RSC Adv.* **2018**, *8*, 31311–31321.
19. Tahmasbi, L.; Sedaghat, T.; Motamedi, H.; Kooti, M. Mesoporous silica nanoparticles supported copper(II) and nickel(II) Schiff base complexes: Synthesis, characterization, antibacterial activity and enzyme immobilization. *J. Solid. State Chem.* **2018**, *258*, 517–525.

20. Marcelo, G.A.; Duarte, M.P.; Oliveira, E. Gold@mesoporous silica nanocarriers for the effective delivery of antibiotics and bypassing of β-lactam resistance. *SN Appl. Sci.* **2020**, *2*, 1354.
21. Montero-Oleas, A.; Ricci, M.L.M.; Ortiz, G.P.; Trens, P.; Roupioz, Y.; Kodjikian, S.; Marchi, M.C.; Cattoën, X.; Bilmes, S.A. One-pot synthesis of core–shell au@mSiO$_2$ nanoparticles for photothermal applications. *ACS Appl. Nano Mater.* **2025**, *8*, 3631–3645.
22. Su, Y.; Mao, Y.; Wu, S.; Liu, L.; Wen, S. Silica coated upconversion nanoplatform for Ag-based chemo-/photodynamic therapy against drug-resistant bacteria. *ACS Appl. Nano Mater*. **2023**, *6*, 8685–8694.
23. Bogdanović, U.; Lazić, V.; Vodnik, V.; Budimir, M.; Marković, Z.; Dimitrijević, S. Copper nanoparticles with high antimicrobial activity. *Mater. Lett.* **2014**, *128*, 75–78.
24. Bogdanović, U.; Vodnik, V.V.; Mitrić, M.; Dimitrijević, S.; Škapin, D.S.; Žunič, V.; Budimir, M.; Stoiljković, M. Nanomaterial with high antimicrobial efficacy—Copper/polyaniline nanocomposite. *ACS Appl. Mater. Interfaces* **2015**, *7*, 1955–1966.
25. Vukoje, I.; Lazić, V.; Vodnik, V.; Mitrić, M.; Jokić, B.; Ahrenkiel, S.P.; Nedeljković, J.M.; Radetić, M. The influence of triangular silver nanoplates on antimicrobial activity and color of cotton fabrics pretreated with chitosan. *J. Mater. Sci.* **2014**, *49*, 4453–4460.
26. Shaikh, S.; Nazam, N.; Rizvi, M.S.; Ahmad, K.; Baig, H.M.; Lee, J.E.; Choi, I. Mechanistic insights into the antimicrobial actions of metallic nanoparticles and their implications for multidrug resistance. *Int. J. Mol. Sci.* **2019**, *20*, 2468.
27. Gisbert-Garzarán, M.; Vallet-Regí, M. Influence of the surface functionalization on the fate and performance of mesoporous silica nanoparticles. *Nanomaterials* **2020**, *10*, 916.
28. Slowing, I.I.; Trewyn, B.G.; Lin, V.S.-Y. Effect of surface functionalization of MCM-41-type mesoporous silica nanoparticles on the endocytosis by human cancer cells. *J. Am. Chem. Soc.* **2006**, *128*, 14792.
29. Selvakannan, P.R.; Mantri, K.; Tardio, J.; Bhargava, S.K. High surface area Au–SBA-15 and Au–MCM-41 materials synthesis: Tryptophan amino acid mediated confinement of gold nanostructures within the mesoporous silica pore walls. *J. Colloid. Interface Sci.* **2013**, *394*, 475–484.
30. Shinde, S.K.; Kim, D.Y.; Saratale, R.G.; Kadam, A.A.; Saratale, G.D.; Syed, A.; Bahkali, A.H.; Ghodake, G.S. Histidine functionalized gold nanoparticles for screening aminoglycosides and nanomolar level detection of streptomycin in water, milk, and whey. *Chemosensors* **2021**, *9*, e358.
31. Shumi, G.; Demissie, T.B.; Eswaramoorthy, R.; Bogale, R.F.; Kenasa, G.; Desalegn, T. Biosynthesis of silver nanoparticles functionalized with histidine and phenylalanine amino acids for potential antioxidant and antibacterial activities. *ACS Omega* **2023**, *8*, 24371–24386.
32. Zhu, H.; Wu, K.; He, C. Continuous Synthesis of Uniformly Dispersed Mesoporous SBA-15 Supported Silver Nanoparticles in a Coiled Flow Inverter Reactor. *Front. Chem.* **2021**, *9*, 747105.
33. Vinoba, M.; Lim, K.S.; Lee, S.H.; Jeong, S.K.; Alagar, M. Immobilization of human carbonic anhydrase on gold nanoparticles assembled onto amine/thiol-functionalized mesoporous SBA-15 for biomimetic sequestration of $CO_2$. *Langmuir* **2011**, *27*, 6227–6234.
34. Liu, J.; Li, S.; Fang, Y.; Zhu, Z. Boosting antibacterial activity with mesoporous silica nanoparticles supported silver nanoclusters. *J. Colloid Interface Sci.* **2019**, *555*, 470–479.
35. Liong, M.; France, B.; Bradley, K.A.; Zink, J.I. Antimicrobial activity of silver nanocrystals encapsulated in mesoporous silica nanoparticles. *Adv. Mater.* **2009**, *21*, 1684–1689.
36. Joardar, S.; Adams, M.L.; Biswas, R.; Deodhar, G.V.; Metzger, K.E.; Deweese, K.; Davidson, M.; Richards, R.M.; Trewyn, B.G.; Biswas, P. Direct synthesis of silver nanoparticles modified spherical mesoporous silica as efficient antibacterial materials. *Micropor. Mesopor. Mat.* **2021**, *313*, 110824.
37. Lodeiro, A.F.; Djafari, J.; Lodeiro, J.F.; Duarte, M.P.; Mauricio, E.M.; Martínez, J.L.C.; Lodeiro, C. Synthesis of mesoporous silica coated gold nanorods loaded with methylene blue and its potentials in antibacterial applications. *Nanomaterials* **2021**, *11*, 1338.
38. Tian, Y.; Qi, J.; Zhang, W.; Cai, Q.; Jiang, X. Facile, One-pot synthesis, and antibacterial activity of mesoporous silica nanoparticles decorated with well-dispersed silver nanoparticles. *ACS Appl. Mater. Interfaces* **2014**, *6*, 12038−12045.
39. Alshareef, A.; Laird, K.; Cross, R.B.M. Shape-dependent antibacterial activity of silver nanoparticles on *Escherichia coli* and *Enterococcus faecium* bacterium. *App. Surf. Sci*. **2017**, *424*, 310–315.
40. Hameeda, S.; Wanga, Y.; Zhaoa, L.; Xiea, L.; Yinga, Y. Shape-dependent significant physical mutilation and antibacterial mechanisms of gold nanoparticles against foodborne bacterial pathogens (*Escherichia coli*, *Pseudomonas aeruginosa* and *Staphylococcus aureus*) at lower concentrations. *Mater. Sci. Eng. C* **2020**, *108*, 110338.
41. Kokunešoski, M.; Gulicovski, J.; Matović, B.; Logar, M.; Milonjić, S.K.; Babić, B. Synthesis and surface characterization of ordered mesoporous silica SBA-15. *Mater. Chem. Phys.* **2010**, *124*, 1248–1252.

42. Kokunešoski, M.; Baščarević, Z.; Rakočević, Z.; Šaponjić, A.; Šaponjić, Đ.; Jordanov, D.; Babić, B. Influence of synthesis conditions on morphological features of the SBA-15 containing only elongated and rounded/spherical grains. *Sci. Sinter.* **2018**, *50*, 111–121.
43. Barret, E.P.; Joyner, L.G.; Halenda, P.P. The determination of pore volume and area distributions in porous substances. I. computations from nitrogen isotherms. *J. Am. Chem. Soc*. **1951**, *73*, 373–380.
44. Lippens, B.C.; Linsen, B.G.; de Boer, J.H. Studies on pore systems in catalysts I. The adsorption of nitrogen; apparatus and calculation. *J. Catalysis* **1964**, *3*, 32–37.
45. Oszust, M.; Gdula, K.; Borowski, P.; Dąbrowski, A.; Barczak, M. Adsorption of L-histidine onto functionalized mesoporous SBA-15 organosilicas. *Adsorpt. Sci. Technol*. **2015**, *33*, 669–676.
46. Bag, S.; Rauwolf, S.; Suyetin, M.; Schwaminger, S.P.; Wenzel, W.; Berensmeier, S. Buffer Influence on the Amino Acid Silica Interaction. *ChemPhysChem* **2020**, *21*, 2347–2356.
47. Vlasova, N.; Golovkova, L. The adsorption of amino acids on the surface of highly dispersed silica. *Colloid. J.* **2004**, *66*, 657–662.
48. Guo, C.; Holland, G.P. Alanine Adsorption and Thermal Condensation at the Interface of Fumed Silica Nanoparticles: A Solid-State NMR Investigation**.** *J. Phys. Chem*. *C* **2015**, *119*, 25663–25672.
49. Iswarya, C.N.; Daniel, S.C.G.K.; Sivakumar, M. Studies on L-histidine capped Ag and Au nanoparticles for dopamine detection. *Mat. Sci. Eng. C* **2017**, *75*, 393–401.
50. Kumari, M.M.; Jacob, J.; Philip, D. Green synthesis and applications of Au–Ag bimetallic nanoparticles. *Spectrochim. Acta A* **2015**, *137*, 185–192.
51. Cai, W.; Zhang, L. Ambience-induced alternating change of optical absorption for the porous silica host loaded with silver nanometer particles. *Appl. Phys. A* **1998**, *66*, 419–422.
52. Lerme, J.; Palpant, B.; Prevel, B.; Pellarin, M.; Treilleux, M.; Vialle, J.L.; Perez, A.; Broyer, M. Quenching of size effects in free and matrix-embedded silver clusters. *Phys. Rev. Lett.* **1998**, *80*, 5105–5108.
53. Sun, Y.; Mayer, B.; Xia, Y. Template-engaged replacement reaction: A one-step approach to the large-scale synthesis of metal nanostructures with hollow interiors. *Nano Lett.* **2002**, *2*, 481–485.
54. Au, L.; Lu, X.; Xia, Y. A comparative study of galvanic replacement reactions involving Ag nanocubes and $AuCl^{2-}$ or $AuCl^{4-}$. *Adv. Mater*. **2008**, *20*, 2517–2522.
55. Andrews, K.W.; Dyson, D.J.; Keown, S.R. *Interpretation of Electron Diffraction Patterns*; Springer: New York, NY, USA, 1967.
56. Sing, K.S.W.; Everett, D.H.; Haul, R.A.W.; Moscou, L.; Pierotti, R.A.; Rouquerol, J.; Siemieniewska, T. Reporting physisorption data for gas/solid systems with special reference to the determination of surface area and porosity. *Pure Appl. Chem.* **1985**, *57*, 603–619.
57. Lowell, S.; Shields, J.E.; Thomas, M.A.; Thommes, M. *Charactrization of Porous Solids and Powders: Surface Area, Pore Size and Density*; Kluwer Academic Publishers: Dordrecht, The Netherlands, 2004; p. 44.
58. Niroumand, U.; Firouzabadi, N.; Goshtasbi, G.; Hassani, B.; Ghasemiyeh, P.; Mohammadi-Samani, S. The effect of size, morphology and surface properties of mesoporous silica nanoparticles on pharmacokinetic aspects and potential toxicity concerns. REVIEW article. *Front. Mater. Sec. Polym. Compos. Mater.* **2023**, *10*, 1189463.https://doi.org/10.3389/fmats.2023.1189463.
59. Nhat, T.V.; Astam, K.P.; Dukjoon, K. Pore size and concentration effect of mesoporous silica nanoparticles on coefficient of thermal expansion and optical transparency of poly(ether sulfone) film. *Phys. Chem. Chem*. **2016**, *19*, 1937–1944. https://doi.org/10.1039/c6cp07545b.
60. Sareen, S.; Mutreja, V.; Singha, S.; Pal, B. Highly dispersed Au, Ag and Cu nanoparticles in mesoporous SBA-15 for highly selective catalytic reduction of nitroaromatics. *RSC Adv.* **2015**, *5*, 184–190.
61. Abbasi, B.A.; Iqbal, J.; Nasir, J.A.; Zahra, S.A.; Shahbaz, A.; Uddin, S.; Hameed, S.; Gul, F.; Kanwal, S.; Mahmood, T. Environmentally friendly green approach for the fabrication of silver oxide nanoparticles: Characterization and diverse biomedical applications. *Microsc. Res. Techn*. **2020**, *83*, 1308–1320.
62. Yasuda, T.; Komiyama, H.; Tanaka, K. Gas-sensitive electrical-conduction and its mechanism in a Ag/insulator system with locally discontinuous structure. *Jpn. J. Appl. Phys.* **1987**, *26*, 818–824.
63. Cai, W.; Tan, M.; Wang, G.; Zhang, L. Reversible transition between transparency and opacity for porous silica host dispersed with silver nanometer particles within its pores. *Appl. Phys. Lett*. **1996**, *69*, 2980–2982.
64. Le Bail, A.; Duroy, H.; Fourquet, J.L. Ab-initio structure determination of $LiSbWO_6$ by X-ray powder diffraction. *Mater. Res. Bull.* **1988**, *23*, 447–452.
65. Rodríguez-Carvajal, J. Recent advances in magnetic structure determination by neutron powder diffraction. *Phys. B Condens. Matter* **1993**, *192*, 55–69.

66. Roy, B.; Baier, F.; Rosin, A.; Gerdes, T.; Schafföner, S. Structural characterization of the near-surface region of soda–lime–silica glass by X-ray photoelectron spectroscopy. *Int. J. Appl. Glass. Sci.* **2023**, *14*, 229–239.
67. Oliveira, C.; Chaves, C.R.; Bargiela, P.; da Graça Carneiro da Rocha, M.; da Silva, A.F.; Chubaci, J.F.D.; Boström, M.; Persson, C.; Malta, M. Surface studies of the chemical environment in gold nanorods supported by X-ray photoelectron spectroscopy (XPS) and ab initio calculations. *J. Mater. Res. Technol.* **2021**, *15*, 768–776.
68. Pugazhendhi, A.; Prabakar, D.; Jacob, J.M.; Karuppusamy, I.; Saratale, R.G. Synthesis and characterization of silver nanoparticles using Gelidium amansii and its antimicrobial property against various pathogenic bacteria. *Microb. Pathog.* **2018**, *114*, 41–45.
69. Wang, L.; Hu, C.; Shao, L. The antimicrobial activity of nanoparticles: Present situation and prospects for the future. *Int. J. Nanomed.* **2017**, *12*, 1227–1249.
70. Okkeh, M.; Bloise, N.; Restivo, E.; De Vita, L.; Pallavicini, P.; Visai, L. Gold Nanoparticles: Can They Be the Next Magic Bullet for Multidrug-Resistant Bacteria? *Nanomaterials* **2021**, *11*, 312.
71. Skłodowski, K.; Chmielewska-Deptuła, S.J.; Piktel, E.; Wolak, P.; Wollny, T.; Bucki, R. Metallic Nanosystems in the Development of Antimicrobial Strategies with High Antimicrobial Activity and High Biocompatibility. *Int. J. Mol. Sci.* **2023**, *24*, 2104.
72. Bogdanović, U.; Dimitrijević, S.; Škapin, D.S.; Popović, M.; Rakočević, Z.; Leskovac, A.; Petrović, S.; Stoiljković, M.; Vodnik, V. Copper-polyaniline nanocomposite: Role of physicochemical properties on the antimicrobial activity and genotoxicity evaluation. *Mat. Sci. Eng. C* **2018**, *93*, 49–60.
73. Stamenović, U.; Davidović, S.; Petrović, S.; Leskovac, A.; Stoiljković, M.; Vodnik, V. Antimicrobial and biological effects of polyaniline/polyvinylpyrrolidone nanocomposites loaded silver nanospheres/triangles. *New J. Chem.* **2021**, *45*, 12711–12720.
74. Makabenta, J.M.V.; Nabawy, A.; Li, C.H.; Malan, S.S.; Patel, R.; Rottello, V.M. Nanomaterial-based therapeutics for antibiotic-resistant bacterial infections. *Nat. Rev. Microbiol.* **2021**, *19*, 23–36.
75. Naseem, T.; Waseem, M. A comprehensive review on the role of some important nanocomposites for antimicrobial and wastewater applications. *Int. J. Environ. Sci. Technol.* **2022**, *19*, 2221–2246.